HiSST: 3rd International Conference on
High-Speed Vehicle Science Technology
14 -19 April 2024, Busan, Korea

Numerical Analysis of Confined Supersonic Combustion Fueled via a Fluidic Oscillator

G. Pelletier[1]

Abstract

Reactive Delayed Detached Eddy Simulations (DDES) were performed to investigate the effects of oscillatory hydrogen injection into a confined transverse supersonic flow of vitiated air. The corresponding experimental conditions were studied in the LAPCAT-II combustor, operating in the LAERTE facility at the ONERA Palaiseau Research Center. The core concept underlying this investigation revolves around the application of a fluidic oscillator, a device capable of inducing oscillatory motion in fluid flow, devoid of any mechanical components. In this context, oscillatory injection is harnessed to enhance the mixing efficiency within the combustor. Moreover, the study delves into another effect of the fluidic oscillator, the ability of sweeping injection to delay the onset of thermal choking within the combustor. This phenomenon has been identified as closely related to a specific structural interaction involving the boundary layer, shockwaves, and combustion processes. Improved mixing of fresh gases is demonstrated to mitigate this phenomenon, thus extending the operational envelope of the scramjet engine. The primary focus of this paper centers on the combustor's response to various fluidic oscillators, encompassing a range sweeping angles. Comparative assessments of mixing and combustion efficiencies are conducted.

Keywords: Supersonic C*ombustion; Fluidic Oscillator; Scramjet*

Nomenclature

Latin
e – Internal energy ($J \cdot kg^{-1}$)
k – turbulent kinetic energy ($m^2 \cdot s^{-2}$)
T – Temperature (K)
P – Pressure (Pa)
u – flow velocity ($m \cdot s^{-1}$)
x, y, z – cartesian coordinates (mm)
Y – mass fraction (-)

Greek
μ – Dynamic viscosity $kg \cdot m^{-1} \cdot s^{-1}$
ν – kinematic viscosity ($m^2 \cdot s^{-1}$)
τ – viscous stress tensor (Pa)
Φ – Equivalence ration (-)
η – Combustion efficiency (-)
ω – Pseudo-dissipation (s^{-1})
$\dot{\omega}$ – Species production rate (s^{-1})

Subscripts
0 – Stagnation values
α – Relative to the species

Superscript
+ – Relative to the wall coordinates

1. Description of the experimental set-up

The LAPCAT-II combustor is fed with a hot vitiated air-stream at Mach 2 issued from a Laval nozzle. This vitiated air-stream is generated through a preliminary combustion of H_2-air and subsequent replenishment of O_2 to uphold the oxygen molar fraction at 0.21. The inlet stagnation temperature is

[1] *ONERA, Université Paris Saclay, F-91123 Palaiseau – France ; guillaume.pelletier@onera.fr*

adjustable within the range of 1300-1900 K, accompanied by a variable stagnation pressure spanning from 0.1 to 1.2 MPa.

The combustor is characterized by a constant width of 40 mm and is composed of four consecutive sections. The initial section — isolator — maintains a uniform cross-sectional area with an inlet height of 35.4 mm and a length of 215 mm. Subsequent to the isolator, there are three additional sections distinguished by diverging half angles, specifically one degree (318 mm length), three degrees (354.5 mm length), and again one degree (305 mm length), designed to prevent thermal choking. The total length of the combustor, including the spacing between the nozzle exit and the isolator inlet, is 1257 mm. It features large optical accesses, which allow optical diagnostics to be settled. The corresponding diagnostics include single-point measurements and imaging techniques, i.e., shadowgraphy or Schlieren, and planar Laser-induced fluorescence (PLIF) [1]. The Laval nozzle is used to generate supersonic flow conditions at the combustor inlet. Figure 1 depicts the profile of the Mach 2 Laval nozzle together with the combustor geometry. The position x = 0 mm corresponds to the nozzle throat.

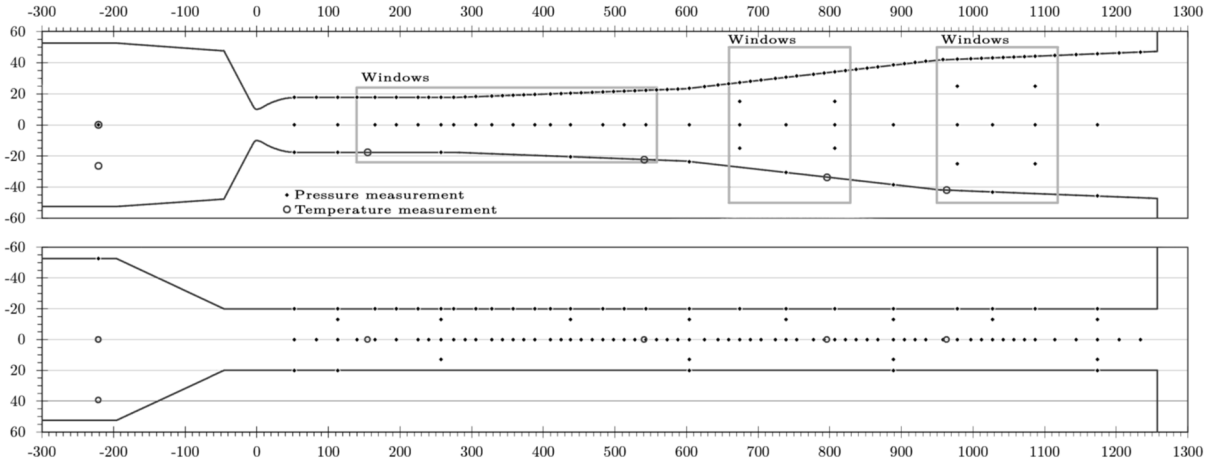

Figure 1 Geometry of the LAPCAT-II combustor

The combustion chamber is made of a copper alloy, and its inner walls include a 300 μm thick thermal barrier coating (TBC) made of Yttria-stabilized Zirconia (Yttria denotes Yttrium oxide). The TBC surface, resembling sandpaper, has been subjected to characterization through scanning electron microscopy (SEM), revealing an average characteristic roughness of 65 μm. Hydrogen injection into the primary supersonic flow of vitiated air is achieved through two 2 mm diameter holes positioned at x = 200 mm along the middle of the top and bottom walls of the test section, as illustrated in Figure 1. Measurements of fuel pressure and temperature are conducted 104 mm upstream from the corresponding injection port.

The LAPCAT-II combustion chamber has undergone a detailed examination of two distinct combustion cases (refer to Table 1). This investigation provides insights into the intricate mechanisms governing the transition from a supersonic combustion regime to a partially thermally choked combustion state. Details of this transition mechanism have been previously documented in [1].

Table 1 Experimental cases

Ref.	T_0 (K)	Φ	Comment
Case A	1700	0.121	Supersonic Combustion
Case B	1700	0.145	Partially Thermally Chocked Combustion

The primary objective of this study is to evaluate the impact of making use of fluidic oscillators in order to inject hydrogen. To achieve this goal, the two sets of experimental conditions, labeled as cases A and B, will be used as a basis of comparison. The comprehensive characteristics of these two cases are provided in Table 2. Within this table, the subscript "j" pertains to the hydrogen injection conditions,

whereas the remaining parameters are associated with the primary vitiated air flow originating from the Laval nozzle.

Table 2 Experimental conditions

Ref.	P_0 (bar)	T_0 (K)	Y_{N2}	Y_{O2}	Y_{H2O}	$P_{t,j}$ (bar)	$T_{t,j}$ (K)	Φ
Case A	4,03	1700	0,5775	0,2554	0,1671	3,91	305	0.121
Case B	4,07	1700	0,5852	0,2476	0,1672	4,78	300	0.145

Figure 6 depicts the instantaneous OH∗ chemiluminescence emission overlaid on Schlieren imaging for cases A (left) and B (right), as described in [1]. The combination of OH∗ chemiluminescence and Schlieren imaging allows for the observation of both the reaction zones and the surrounding shock structure.

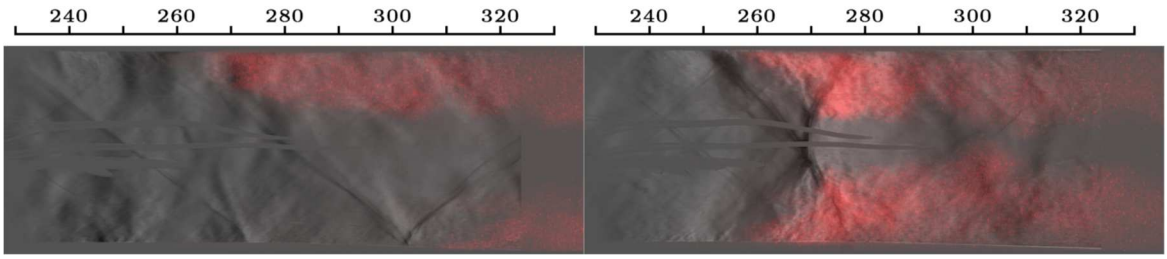

Figure 2 OH* visualization superimposed on schlieren images for cases A (left) and B (right).

As emphasized in reference [1,2], the injection of hydrogen at x = 200 mm induces shock reflections, visually depicted in grayscale in Figure 2, especially for case A. As detailed in [3], both cases A and B manifest distinct combustion modes. Case A is associated with a supersonic weak combustion mode driven by self-ignition processes, while case B is associated with a partially choked combustion mode where heat release is correlated with significant modifications of the compressible flowfield.

2. Description of the inlet oscillator

In this study, computational analyses of fluidic oscillators (refer to Figure 3) are performed to assess the fundamental characteristics achievable within the LAPCAT-II combustion chamber. The design used in this study draws inspiration from [4].

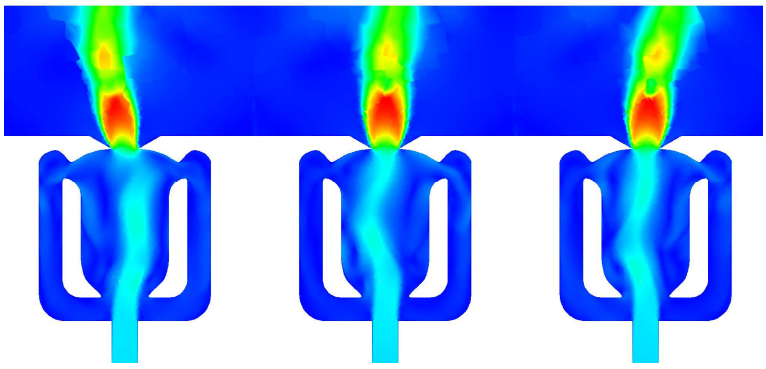

Figure 3 Principle of a fluidic oscillator

A fluidic oscillator, also known as a sweeping jet actuator (Figure 3), introduces a vibrating flow continuously injecting oscillating jets, effectively distributing the fuel over a wider area. The angle and frequency of the sweeping jet at the exit of the fluidic oscillator are contingent on the internal shape.

Preliminary computational analyses conducted on the design depicted in Figure 3 revealed that the shape explored had an oscillation frequency and sweeping angle of approximately 20 kHz and 15°, respectively. The outlet conditions of this simulation are linked to the hydrogen inlet of the LAPCAT-II

chamber. Additionally, further investigations involve exploring sweeping angle conditions with a 30° sweeping angle.

3. Computational Model

The present study is conducted with the ONERA computational fluid dynamics code CEDRE [5] which is a multi-physics platform relying on specific solvers to handle complex flow simulations. Specifically, this study harnesses the capabilities of the finite volume three-dimensional compressible and reactive Navier-Stokes solver CHARME.

The set of governing equations corresponds to the compressible form of the Navier-Stokes equations. It includes balance equations for mass, momentum, energy, and species mass fractions as follows:

$$\frac{\partial \bar{\rho}}{\partial t} + \frac{\partial}{\partial x_j}\bar{\rho}\tilde{u}_j = 0$$

$$\frac{\partial}{\partial x_j}\bar{\rho}\tilde{u}_i + \frac{\partial}{\partial x_j}\bar{\rho}\tilde{u}_j\tilde{u}_i = \frac{\partial}{\partial x_j}\left(-\left(\overline{\rho u_j u_\iota} - \bar{\rho}\tilde{u}_j\tilde{u}_i\right) - \bar{P}\delta_{ij} + \bar{\tau}_{ij}\right)$$

$$\frac{\partial}{\partial x_j}\bar{\rho}\tilde{e}_t + \frac{\partial}{\partial x_j}\bar{\rho}\tilde{u}_j\tilde{e}_t = \frac{\partial}{\partial x_j}\left(-\left(\overline{\rho u_j e_t} - \bar{\rho}\tilde{u}_j\tilde{e}_t\right) - \bar{J}_j^{e_t}\delta_{ij} + \tilde{\sigma}_{ij}\tilde{u}_i\right)$$

$$\frac{\partial}{\partial x_j}\bar{\rho}\tilde{Y}_\alpha + \frac{\partial}{\partial x_j}\bar{\rho}\tilde{u}_i\tilde{Y}_\alpha = \frac{\partial}{\partial x_j}\left(-\left(\overline{\rho u_\iota Y_\alpha} - \bar{\rho}\tilde{u}_i\tilde{Y}_\alpha\right) - \bar{J}_j^{Y_\alpha}\right) + \bar{\dot{\omega}}_\alpha$$

where ρ denotes the density, u_i is the i-component of the velocity field, e_t is the total energy per unit mass, Y_α is the mass fraction of chemical species α and $P = \rho RT/W$ – with W the molar weight of the mixture and R the universal gas constant – denotes the pressure. The viscous stress tensor is $\bar{\tau}_{ij} = \mu(\partial u_i/\partial x_j + \partial u_j/\partial x_j) - 2/3\,\mu\,(\partial u_k/\partial x_k)\delta_{ij}$ and $\sigma_{ij} = \tau_{ij} - P\delta_{ij}$. . The unresolved fluxes of mass and energy, i.e., $\overline{\rho u_j u_\iota} - \bar{\rho}\tilde{u}_j\tilde{u}_i$ and $\overline{\rho u_j e_t} - \bar{\rho}\tilde{u}_j\tilde{e}_t$, are deduced from the turbulent diffusivity approximation by introducing turbulent Schmidt and Prandtl numbers, which are set to a standard value of 0.9 [6].

The averaged (or filtered) chemical production rates $\bar{\dot{\omega}}_\alpha$that appear in the right-hand side of the species mass fractions transport equations are represented within the perfectly stirred reactor, i.e., well-stirred reactor (WSR) approach, a modelling framework that neglects the possible influence of unresolved composition fluctuations at the resolved level, i.e, $\bar{\dot{\omega}}_\alpha = \dot{\omega}_\alpha(\tilde{T}, \tilde{Y}_\alpha)$. Such a simplification is commonly retained in high-speed combustion simulations and it must be emphasized that, in the present conditions, combustion has indeed been shown to be chemistry-controlled with maximum values of the heat release rate (HRR) taking place in the turbulent combustion regimes relevant to slow chemistry [7]. In the present study, the description of the corresponding chemical kinetics is based on hydrogen/air chemical scheme of Jachimowski [8].

In this study, hybrid RANS-LES model is not only retained to take advantage of mesh-coarsening in the wall vicinity – and savings in computational time – but also to consider wall roughness thanks to a model that has been developed within the RANS context via the modification of the length scale ℓ_{RANS} involved in the RANS closure, which is replaced by $\ell_{DES} = \min(\ell_{RANS}, C_{DES}\Delta)$ where Δ denotes the mesh cell characteristic size and C_{DES} is a modelling constant. In the vicinity of walls, where $\Delta x^+ \approx \Delta z^+ \gg \Delta y^+$, this formulation leads to $\ell_{DES} = \mathrm{l}_{RANS}$ and the RANS model is recovered, whereas, far from the walls, we have $\ell_{DES} = C_{DES}\Delta$; the model becomes grid-dependent and behaves as a SGS version of the RANS model.

The above formulation is refined within the DDES framework in order to account for the grid-induced separation (GIS) phenomena [9,10] and the length scale is defined as: $\ell_{DDES} = \mathrm{l}_{RANS} - \mathrm{f}_{\mathrm{DDES}}\cdot\max(0, l_{RANS} - C_{DES}\Delta)$ where $\mathrm{f}_{\mathrm{DDES}}$ is a shielding function designed to be unity in the LES region and zero elsewhere. Depending on the turbulence model, several expressions have been proposed in the literature for $\mathrm{C}_{\mathrm{DES}}$ and $\mathrm{f}_{\mathrm{DDES}}$ [10]. In the present study, the hybridization follows the DDES framework [10] and Strelets' extension brought to the Menter's k-ω SST turbulence model [11-13].

This turbulence model does involve the following two transport equations for the turbulent kinetic energy (TKE) k and pseudo-dissipation ω.

$$\frac{\partial}{\partial x_j}\bar{\rho}k + \frac{\partial}{\partial x_j}\bar{\rho}\tilde{u}_j k = \frac{\partial}{\partial x_j}\left((\mu + \sigma_k \mu_t)\frac{\partial k}{\partial x_j}\right) + P_k - D_k$$

$$\frac{\partial}{\partial x_j}\bar{\rho}\omega + \frac{\partial}{\partial x_j}\bar{\rho}\tilde{u}_j \omega = \frac{\partial}{\partial x_j}\left((\mu + \sigma_\omega \mu_t)\frac{\partial \omega}{\partial x_j}\right) + P_\omega - D_\omega + 2\bar{\rho}(1 - F_1)\sigma_{\omega 2}\frac{1}{\omega}\frac{\partial k}{\partial x_i}\frac{\partial \omega}{\partial x_i}$$

Where σ_k, σ_ω, β and γ are modeling constants, P_k, P_ω, D_k and D_ω are the production and dissipation which include a slight modification brought to the TKE production term [14].

Within the DDES turbulence modelling framework, the TKE dissipation rate $D_k = \bar{\rho}k^{\frac{3}{2}}/l_{RANS}$ is modified in such a manner that the RANS turbulence length scale ℓ_{RANS} is replaced by ℓ_{DDES}. The shielding function of Fan et al. [15] is presently retained: $\mathrm{f}_{DDES} = 1 - \tanh(\omega^{-1}\max(500\nu/y^2, \sqrt{k}/(\beta^* y)))$. Finally, it should be noted that, following Strelets [13], the value of CDES is deduced from $\mathrm{C}_{DES} = F_1 C_{DES,1} + (1 - F_1)C_{DES,2}$ with $\mathrm{C}_{DES,1} = 0{,}78$ and $\mathrm{C}_{DES,2} = 0{,}61$.

This turbulence model is used in conjunction with a wall roughness model. Notably, this model accounts for the influence of Thermal Barrier Coating (TBC) residual roughness, a crucial factor in replicating the experimental findings [1-3]. The equivalent sand grain model is used to represent the wall roughness effects. The main objective with such a methodology is to render the skin friction increase that is induced by wall roughness. In practice, the corresponding increase can be related to a downward shift of the velocity profile within the logarithmic region of the boundary-layer [16]. To this purpose, the methodology developed by Aupoix et al. [17] retained to proceed with the present set of unsteady simulations.

4. Mesh

The entire computational mesh comprises tetrahedral cells along with prism layers along the walls, totaling approximately 23.4 million cells. Localized refinement is applied in the fuel injection and mixing layer regions to ensure an accurate description of the mixing layer growth rate. In accordance with the guidelines for Delayed Detached Eddy Simulations (DDES), the computational grid undergoes significant refinement, particularly in the shear layers. Practically, insights from previous Reynolds-Averaged Navier-Stokes (RANS) computations on the same geometry were utilized to identify high vorticity zones in the wake of the injection [3]. The corresponding computed field of the vorticity norm has thus been subsequently used to proceed with grid refinement in order to design the computational mesh retained for DDES. Figure 4 provides a view of the resulting computational mesh in the vicinity of the injection and mixing layers.

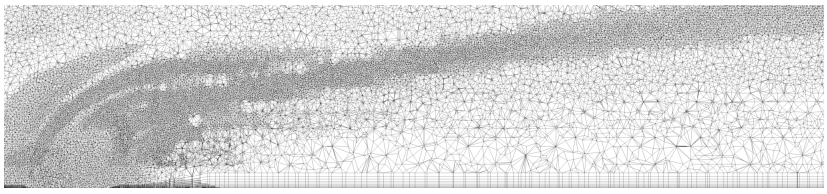

Figure 4 View of the computational mesh in the vicinity of the hydrogen injection port.

The dimensionless height profile y^+ of computational cells situated in close proximity to the wall (in the plane z=0) indicates that, within the region of interest, the values of y^+ remain smaller than unity (see Figure 5).

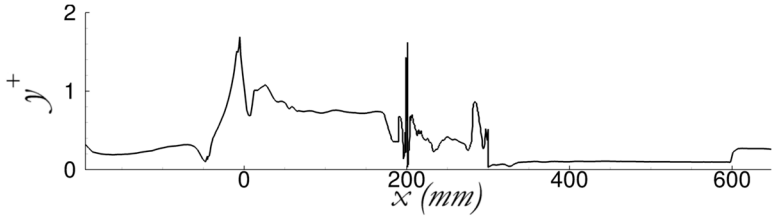

Figure 5 Profile of y^+ in the symmetry plane.

5. Numerical evaluation of the chamber efficiencies

The results are analyzed in terms of energetic performance and efficiencies. These efficiencies characterize the thermo-chemical state in a transverse section of the combustor with respect to the thermo-chemical state issued from an ideal process.

The actual heat release $\dot{Q}$ is defined as the power needed to bring back the outlets products to the temperature and speed of the reactants:

$$\dot{Q} = (H_P + \dot{m}v_P^2/2) - \left(H_P^{T_R} + \dot{m}v_R^2/2\right)$$

with v_R and v_P are the averaged flow velocities of the reactants and products, respectively, H_P the enthalpy flux of the product $H_P = \int_{S_{out}} \rho v \cdot nh(T,Y,p)dS$ where ρ is the density, v the velocity vector, n the surface normal unit vector, and h the static enthalpy per unit mass computed at the static pressure P and static temperature T for a mixture characterized by the mass fraction vector Y. The quantity $H_P^{T_R} = \int_{S_{out}} \rho v \cdot nh(T_R,Y,p)dS$ is the enthalpy flux computed at the reactants temperature T_R defined by $\int_{S_{in}} -\rho v \cdot nh(T_R,Y,p)dS = \int_{S_{in}} -\rho v \cdot nh(T,Y,p)dS$. The mass flow rate is given by $\dot{m} = \int_{S_{in}} \rho v \cdot n\, dS$.

The energy balance between the chamber inlet and outlet is given by: $H_P + \dot{m}v_P^2/2 = H_R + \dot{m}v_R^2/2 - \dot{Q}_w$ with H_R the enthalpy flux of the reactants $\int_{S_{in}} \rho v \cdot nh(T,Y,p)dS$ and $\dot{Q}_w$ the wall heat losses. Thus, the actual heat release writes:

$$\dot{Q} = H_R - H_P^{T_R} - \dot{Q}_w.$$

For an ideal combustion, there would be no wall heat losses and the products would correspond to a homogeneous mixture of fully-oxidized products. Thus, the ideal heat release $\dot{Q}^{id}$ would be $H_R - H_P^{T_R,Y^{id}}$ with $H_P^{T_R,Y^{id}} = \int_{S_{out}} \rho v \cdot nh(T_R,Y^{id},p)dS$ the enthalpy flux computed at temperature T_R with the composition Y^{id}. The combustion chamber efficiency is thus given by

$$\eta_e = \dot{Q}/\dot{Q}^{id} = (H_R - H_P^{T_R} - \dot{Q}_w)/\,(H_R - H_P^{T_R,Y^{id}})\,.$$

The effect of the thermal losses, mixture inhomogeneity, and incomplete oxidation can be discriminated from each others by introducing three distinct efficiencies. The first is the thermal efficiency, which is defined as the ratio between the heat release with and without thermal losses:

$$\eta_{th} = (H_R - H_P^{T_R} - \dot{Q}_w)/\,(H_R - H_P^{T_R})$$

The second is the chemical efficiency, which is the ratio between the heat release without thermal losses and what it would have been with perfectly oxidized products:

$$\eta_{ch} = (H_R - H_P^{T_R})/\,(H_R - H_P^{T_R,Y^{ox}})$$

where $H_P^{T_R,Y^{ox}}$ is the enthalpy flux computed at temperature T_R with the composition Y^{ox} the local ideal composition of the products.

Finally, the last is the mixing efficiency, which corresponds to the ratio between the heat release without wall heat losses obtained with a perfect oxidation of the non-homegenous mixture to the one obtained for a homogeneous (or ideal) mixture:

$$\eta_{mix} = (H_R - H_P^{T_R,Y^{ox}})/\,(H_R - H_P^{T_R,Y^{id}}).$$

Thus, the combustion chamber efficiency can be evaluated from:

$$\eta = \eta_{th} \cdot \eta_{ch} \cdot \eta_{mix}$$

6. Numerical results

6.1. Supersonic Combustion Mode (Case A)

The objective of this section is to assess the effect of a sweeping injection on combustion development and stabilization.
As emphasized in section II.B, combustion stabilizes far downstream of hydrogen inlet in the case A and corresponds to a supersonic combustion mode associated to self-ignition processes following a thermal runaway or induction period Conversely, case B correspond to a partially chocked regime. The initial analysis focuses on case A to observe the influence of the fluidic oscillator on mixing and combustion efficiencies. Subsequently, the study of case B aims to assess the effect of sweeping injection on the choking phenomenon within the chamber.
Figure 6 reports the averaged mixture fraction for the three sweeping angles across four cross-section (i.e., x= 200, 210, 225 and 250 mm). It can be seen that for higher sweeping angle the fuel spread over greater z abscissas. Additionally, a reduced penetration height is observed for the 30° sweeping angle case. To quantify the beneficial impact of the sweeping jet on fuel mixing with the crossflow, the cross-sectional area within the equivalence ratio flammability limit of hydrogen can be assessed. This is illustrated on Figure 7 which highlight an increased surface where fuel and air are well mixed together. The area within the flammability limit of hydrogen is respectively 20% and 40% higher for the 15° and 30° sweeping angle with respect to the reference simulation. Furthermore, as can be observed on Figure 8, the average temperature of the fresh gases within this surface is respectively 7% and 13% higher for the 15° and 30° sweeping angle with respect to the reference simulation. Given that this case is driven by auto-ignition, both the higher local temperature and improved mixing are expected to stimulate combustion ignition.

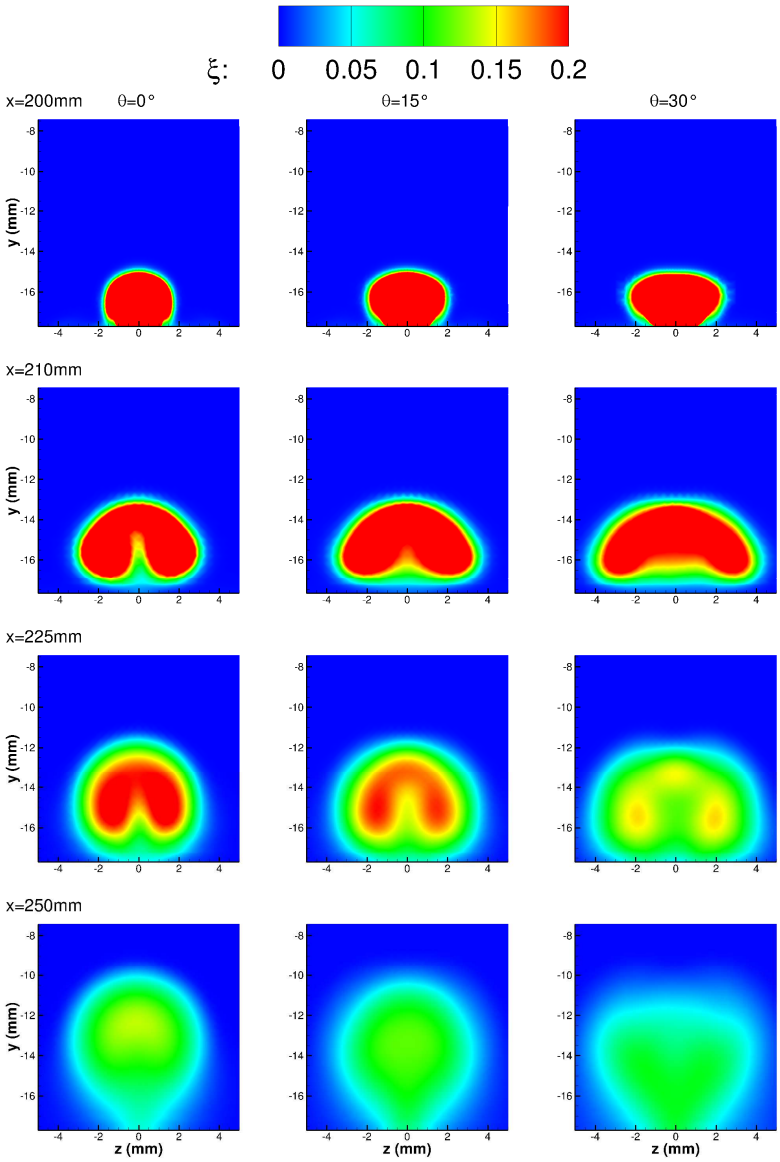

Figure 6 Transverse fields of the averaged mixture ratio for each sweeping angle.

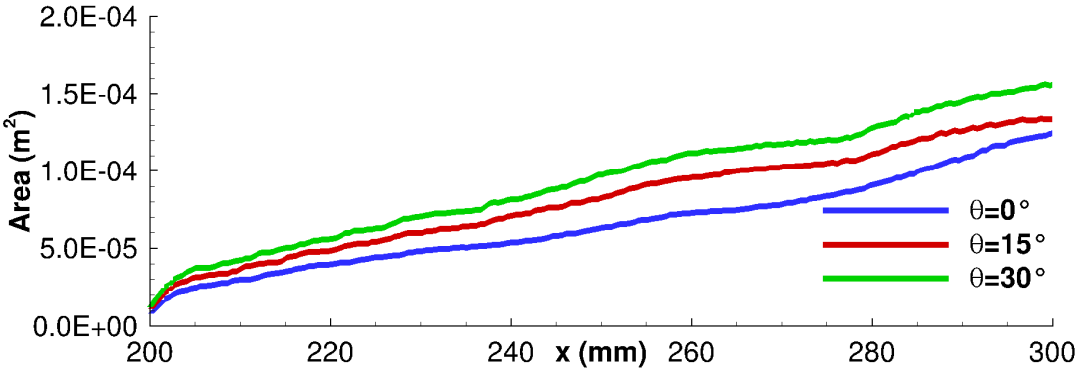

Figure 7 Cross-sectional area within the flammability limit.

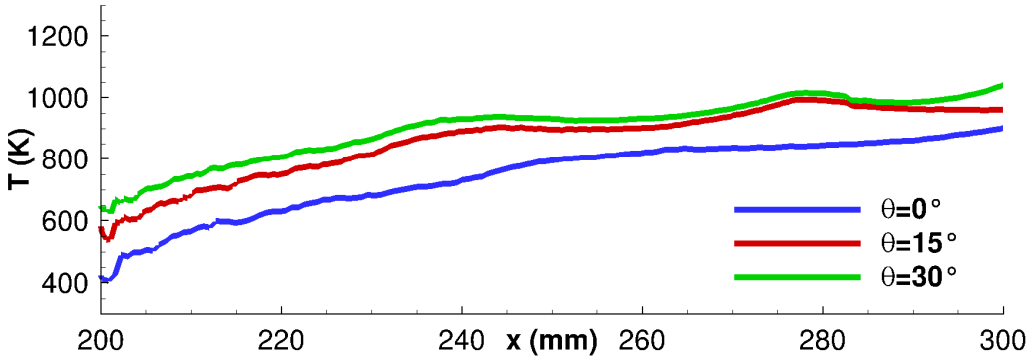

Figure 8 Average temperature of the fluid in the surface within the flammability limit.

Figure 9 illustrates the averaged Heat Release Rate (HRR) fields integrated along the width of the combustor for the three inlet conditions, slightly upstream compared to the no sweeping angle case. This indicates that auto-ignition occurs earlier in the chamber.

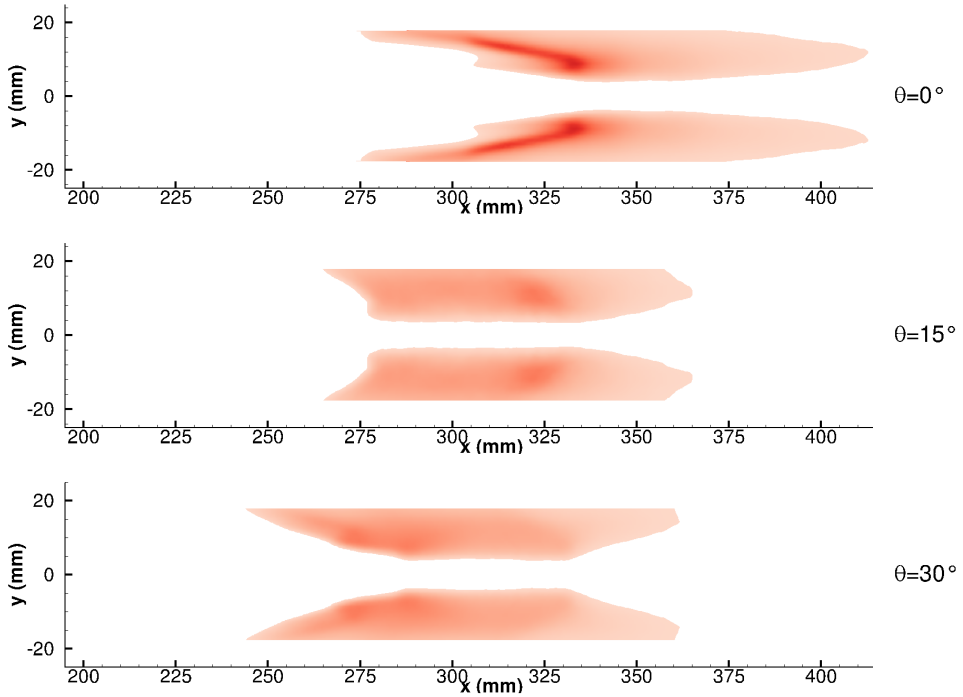

Figure 9 HRR spatially integrated along the combustor width.

The effect of the sweeping inlet condition on mixing and combustion is summarized on Figure 10 where the corresponding efficiencies increases more rapidly in presence of sweeping injection.

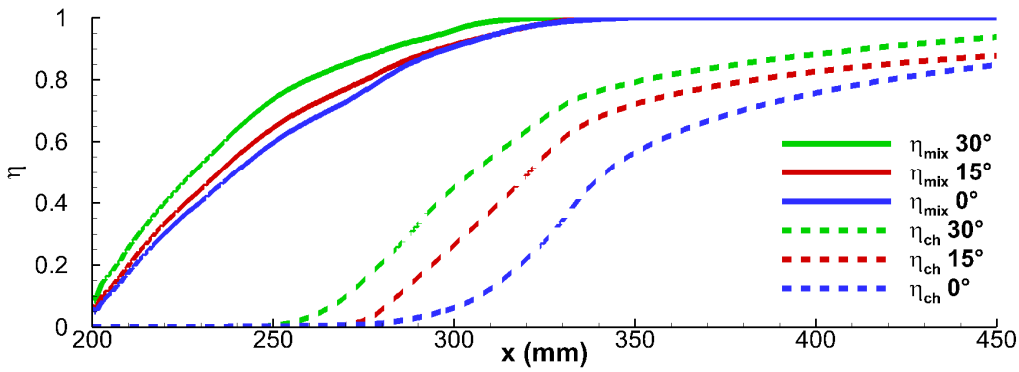

Figure 10 Mixing and chemical efficiencies profiles.

Figure 11 presents the total pressure profile averaged in the cross-section of the chamber. This indicates that another effect of sweeping injection is to increase the total pressure losses within the chamber. In this case, the pressure levels are reduced by 3% and 4% for the 15° and 30° cases, respectively, compared to the reference.

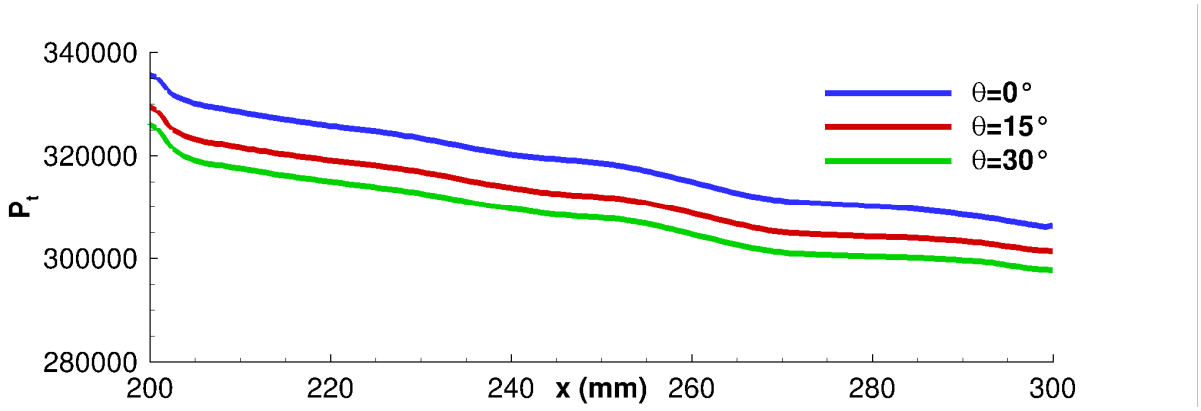

Figure 11 Averaged total pressure profiles.

6.2. Partially Choked Mode (Case B)

This flow topology has been extensively analyzed Ref. [3] and only its main characteristics are briefly reiterated here. The cross-shaped shock structure, observable on Figure 2 is delineated by two regions of massive boundary layer separation. The first region is marked with the two foci of separation, visible at the bottom of Figure 12 either close to the symmetry plane or in the corner of the combustion chamber. The corresponding boundary layer separation phenomena are associated with the adverse pressure gradient that is induced by the cross-shaped shock structure and combustion. The two foci of separation close to the symmetry plane reveal vortical structures featuring a rotation axis normal to the wall. These vortices eject low-momentum fluid into the core flow, thus leading to favorable conditions for ignition development. Combustion processes appear to be quite intense at the cross-shaped shock location.

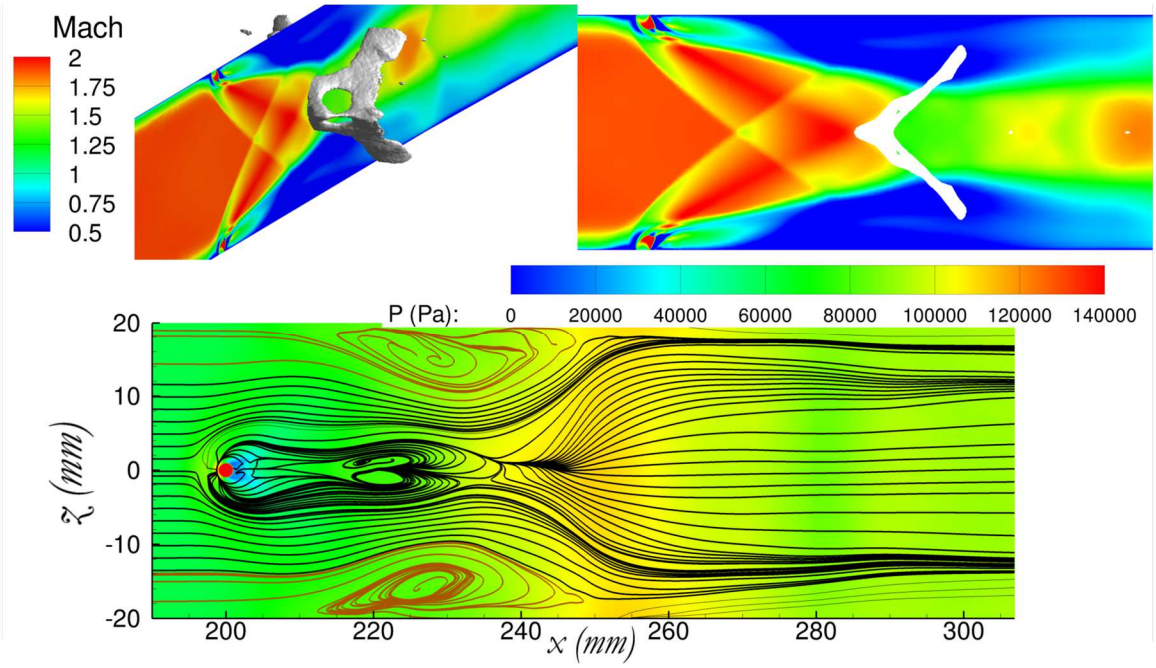

Figure 12 Mach number contours and isosurface of the density gradient (top). Pressure field and streamlines in the plane y^+ 0.1 mm(bottom).

The introduction of oscillating hydrogen injection in this case has a profound effect on Heat Release Rate (HRR), as observed in Figure 13. Transitioning from no oscillation to a 15° sweeping angle moves

combustion further downstream, erasing any trace of the original flow topology. This injection spreads the heat release rate over a broader surface, which in this case stays below the triggering point of the Partially Choked mode and remains in the supersonic combustion mode. Further increases in the sweeping angle follow the same trend as observed in the previous section.

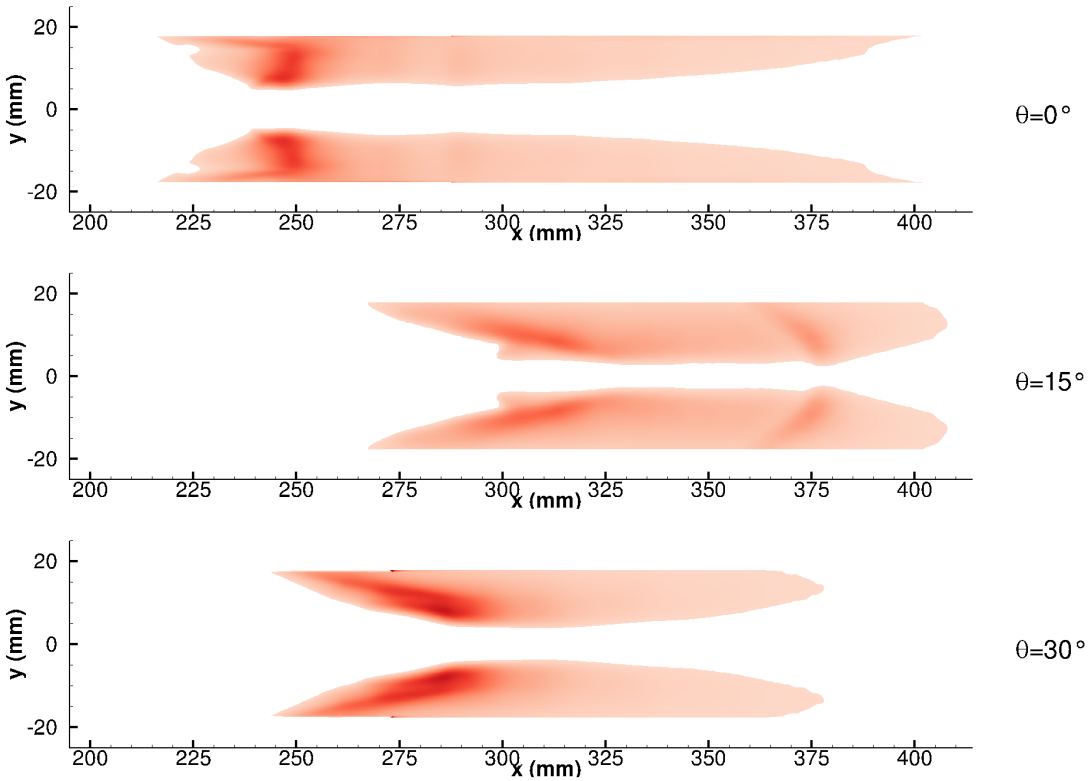

Figure 13 HRR spatially integrated along the combustor width.

7. Conclusion

In this study, the impact of sweeping injection is assessed through numerical simulations on the LAPCAT-II geometry. Two experimental cases have been selected, encompassing a supersonic combustion mode and a Partially Choked regime. Simulations conducted on the first mode reveal an enhancement in mixing and chemical efficiencies at the expense of increased total pressure loss with higher sweeping angles. Simulations on the Partially Choked mode suggest that this mode can be delayed with sweeping injection, allowing for an increase in the maximum global equivalence ratio that can be admitted by the chamber.

References

1. Ristori, A., Brossard, C., and Vincent-Randonnier, A., "Diagnostics optiques des écoulements supersoniques dans une chambre de combustion de statoréacteur mixte au moyen de la strioscopie à haute cadence couplée à la visualisation de l'émission du radical OH*," CFTL 2016, Toulouse, France, 2016
2. Vincent-Randonnier, A., Moule, Y., and Ferrier, M., "Combustion of Hydrogen in Hot Air Flows within LAPCAT-II Dual Mode Ramjet Combustor at Onera-LAERTE Facility - Experimental and Numerical Investigation," AIAA Paper 2014-2932, 2014. https://doi.org/10.2514/6.2014-2932.
3. Pelletier, G., Ferrier, M., Vincent-Randonnier, A., Sabelnikov, V., and Mura, A.: Wall Roughness Effects on Combustion Development in Confined Supersonic Flow. J. Propuls. Power (2020). https://doi.org/10.2514/1.B37842

4. Lee, S., Roh, T.S, Lee, H.J.: Influence of jet parameters of fluidic oscillator-type fuel injector on the mixing performance in a supersonic flow field. Aerosp. Sci. Technol. (2023). https://doi.org/10.1016/j.ast.2023.108154
5. Refloch, A., Courbet, B., Murrone, A., Villedieu, P., Laurent, C., Gilbank, P., Troyes, J., Tessé, L., Chaineray, G., Dargaud, J.-B., Quémerais, E., and Vuillot, F.: CEDRE Software. AerospaceLab Journal, 1–10 (2011)
6. Launder, B. E., and Sharma, B. I., "Application of the Energy-Dissipation Model of Turbulence to the Calculation of Flow Near a Spinning Disc," Letters in Heat and Mass Transfer, Vol. 1, No. 2, 1974, pp. 131–138. https://doi.org/10.1016/0094-4548(74)90150-7.
7. Mura, A., Techer, A., and Lehnasch, G., "Analysis of High-Speed Combustion Regimes of Hydrogen Jet in Supersonic Vitiated Airstream," Combustion and Flame, Vol. 239, May 2022, Paper 111552. https://doi.org/10.1016/j.combustflame.2021.111552
8. Jachimowski, C.: An Analysis of Combustion Studies in Shock Expansion Tunnels and Reflected Shock Tunnels. NASA-TP-3224. (1992). https://ntrs.nasa.gov/api/citations/19920019131/downloads/19920019131.pdf
9. Sagaut, P., Deck, S., and Terracol, M., Multiscale and Multiresolution Approaches in Turbulence, Imperial College Press, London, 2006. https://doi.org/10.1142/p447
10. Spalart, P. R., Deck, S., Shur,M. L., Squires, K. D., Strelets, M. K., and Travin, A., "A New Version of Detached-Eddy Simulation, Resistant to Ambiguous Grid Densities," Theoretical and Computational Fluid Dynamics, Vol. 20, No. 3, 2006, pp. 181–195.
11. Menter, F., "Two-Equation Eddy-Viscosity Transport Turbulence Model for Engineering Applications," AIAA Journal, Vol. 32, No. 8, 1994, pp. 1598–1605. https://doi.org/10.2514/3.12149
12. Menter, F., Kuntz, M., Langtry, R., Hanjalic, K., Nagano, Y., and Tummers, M. J., "Ten Years of Industrial Experience with the SST Turbulence Model," Turbulence Heat and Mass Transfer, Vol. 4, Begell House, New York, 2003, pp. 625–632.
13. Strelets, M. K., "Detached-Eddy Simulation of Massively Separated Flows," AIAA Paper 2001-0879, 2001.
14. Menter, F. R., "Zonal Two Equation k-ω Turbulence Models for Aerodynamic Flows," AIAA Paper 1993-2906, 1993.
15. Fan, C. C., Xiao, X., Edwards, J. R., Hassan, H. A., and Baurle, R. A., "Hybrid Large-Eddy/Reynolds-Averaged Navier-Stokes Simulation of Shock-Separated Flows," Journal of Spacecraft and Rockets, Vol. 41, No. 6, 2004, pp. 897–906.
16. Nikuradse, J., "Law of Flows in Rough Pipes," NACA TM-1292, 1937.
17. Aupoix, B.: Roughness Corrections for the k-ω Shear Stress Transport Model: Status and Proposals. J. Fluids Eng. (2015). https://doi.org/10.1115/1.4028122.
18. Fureby, C.: Large Eddy Simulations of the LAPCAT-II and the SSFE Combustor Configurations. AIAA. (2020). https://doi.org/10.2514/6.2020-1109